Multidimensional position and displacement estimation using periodic coded optical apertures in a single camera imaging system

T Steinmetz[1,*], J Otto[1], H W Pommerenke[1], E Ebert[1], A Kleinwächter[1] and N A Damaschke[1]

1: Institute of General Electrical Engineering, University of Rostock, Germany
*Corresponding author: tino.steinmetz@uni-rostock.de

Keywords: Coded Aperture, Backscattering, Image Processing, Out-of-Focus Imaging

ABSTRACT

Accurately estimating multidimensional positions and displacements in fluid dynamic experiments is essential for understanding complex flow phenomena. This paper presents a novel optical measurement setup capable of determining velocity fields using periodic coded optical apertures in a single-camera imaging system. Our method involves placing a periodic transmission grating in front of the optical system and aligning a laser beam along the system's optical axis. When particles intersect the laser beam, they scatter light, producing out-of-focus images on the imaging sensor resembling the periodic grating. The size and position of these images vary with the distance to the imaging system and the offset from the optical axis, allowing for accurate determination of particle positions. We derive mathematical formulas describing the imaging system and the relationship between image properties and particle positions and verify them through simulations. Additionally, we develop a calibration method enabling arbitrary optical imaging systems to be used with this technique. Finally, we demonstrate the effectiveness of our approach by measuring velocity fields near a ducted ship propeller, a practical application that underscores the real-world impact of our research in fluid dynamics.

1. Introduction

The study of fluid dynamics is indispensable in understanding phenomena ranging from biological flows to industrial processes, and the continual refinement of measurement techniques is crucial. Particle Image Velocimetry (PIV) is a widely used method for measuring velocity fields in fluid dynamics (Raffel et al., 2018), but usually requires more than one optical access window to the measurement volume for separate illumination and image capturing. This paper introduces a new PIV method that requires only a single optical access window by utilizing a backscattering approach combined with out-of-focus coded aperture imaging.

The basic principle of this method relies on the observation that the image of the aperture function of an optical system is scaled in out-of-focus particle images, depending on the distance of the imaged particle from the object plane, as described by Pentland (1987). Further efforts were made by Willert & Gharib (1992) to employ this behavior in a measurement system by utilizing aperture masks consisting of three pinholes within the imaging system (three-pinhole technique). This technique was then further improved and applied in fluid dynamics by Pereira et al. (2000), Pereira & Gharib (2002) and Pereira et al. (2007). However, the three-pinhole technique requires a comparably high computational effort for calibrating the imaging system and determining aperture image positions and sizes.

The approach proposed in this paper reduces the computational complexity of the three-pinhole technique to a more manageable degree. Figure 1 shows the underlying concept of the backscattering architecture.

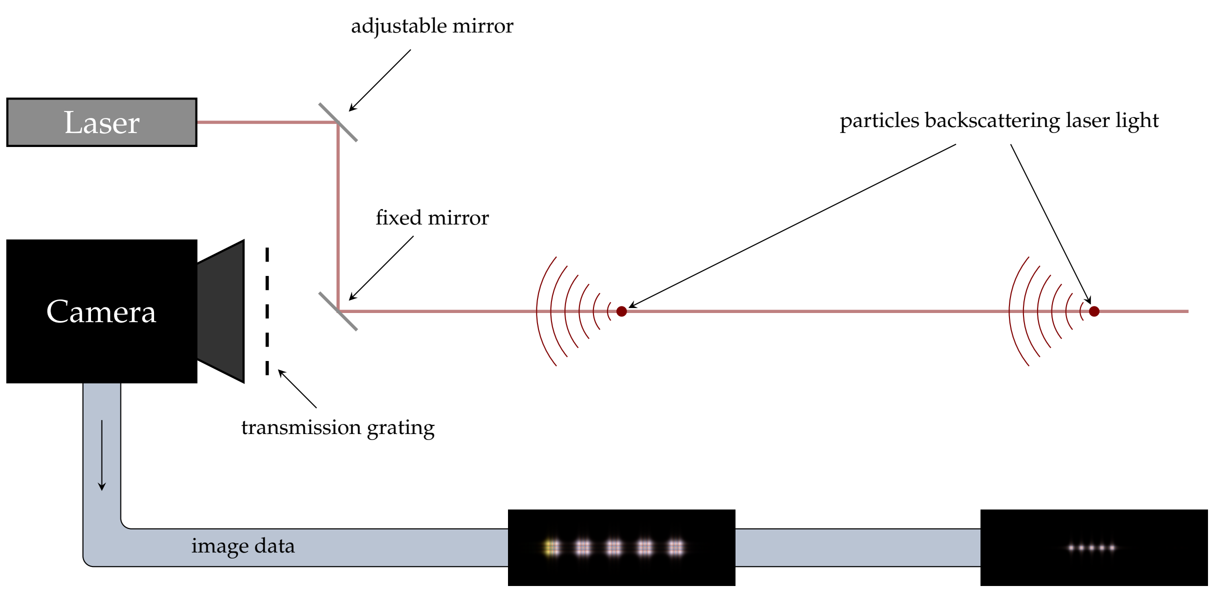

Figure 1. Schematic representation of the measurement system setup.

A laser beam is placed within the optical axis of an imaging system by using two mirrors, one of which is adjustable, aligning the laser beam. A periodic coded aperture mask is placed between the imaging system and the fixed mirror, so light scattered by particles passing through the laser has to pass through it. An offset aperture comparable to Lee et al. (2015) can reduce overlapping between aperture images of particles simultaneously appearing at different distances from the imaging system. Also, the periodic transmission grating has to be aligned with the structure of the imaging sensor, which allows line-wise computation of the resulting image data.

The size of the aperture images is proportional to the period length of the grating function, which the Fast Fourier Transform can efficiently compute. This makes this method suitable to be implemented on a camera platform capable of real-time processing, as demonstrated by Steinmetz et al. (2023).

In this paper, we first introduce periodic coded aperture functions and discuss their spectral properties. Afterward, the optical measurement setup and the theoretical framework behind our method are outlined by deriving mathematical expressions describing the imaging system and the relationship between image properties and particle positions. We are doing this by providing two approaches: one that is more intuitive, based on a single lens setup, and one that is more generalized and applies to imaging systems with arbitrary multi-lens configurations. Next, we present our simulation results to validate the theoretical predictions. Also, we propose a calibration procedure to adapt our method to various optical imaging systems. Finally, we demonstrate the practical application of our approach by conducting real-world measurements of velocity fields near a ducted ship propeller.

2. Periodic Coded Apertures

2.1. Motivation

In conventional imaging systems, a stereoscopic setup is required to perceive depth. By applying the concept of coded optical apertures to the out-of-focus imaging technique, a sense of depth can be realized by evaluating the size of resulting aperture images. This concept has already been built up by Willert & Gharib (1992), who considered an optical aperture with distributed pinholes, leading to the development of the three-pinhole-technique (Pereira et al., 2000). However, those approaches typically require a rather complex setup and computational effort for the localization and evaluation of aperture images. This can be improved by applying aperture functions with a periodic structure aligned with the imaging sensor's pixel array. Then, the size of the aperture image is bound to its period length, which can be determined by utilizing the Fast Fourier Transform (FFT), and the presence of a particle can be determined by evaluating the line and column intensities of the image. As the depth information is encoded in the period length or frequency of the aperture image, this approach can be assigned to the field of compressed sensing.

2.2. Functional Design

Besides improving the spectral properties of the aperture function, the design of a physical aperture mask also requires considerations regarding the placement of one or arrangement of multiple aperture functions within the aperture plane. Those considerations include the desired estimation components, the particle density within the observed environment, and the construction of the measurement system.

Fig. 2 shows different types of apertures considered for evaluating the principles outlined in this work.

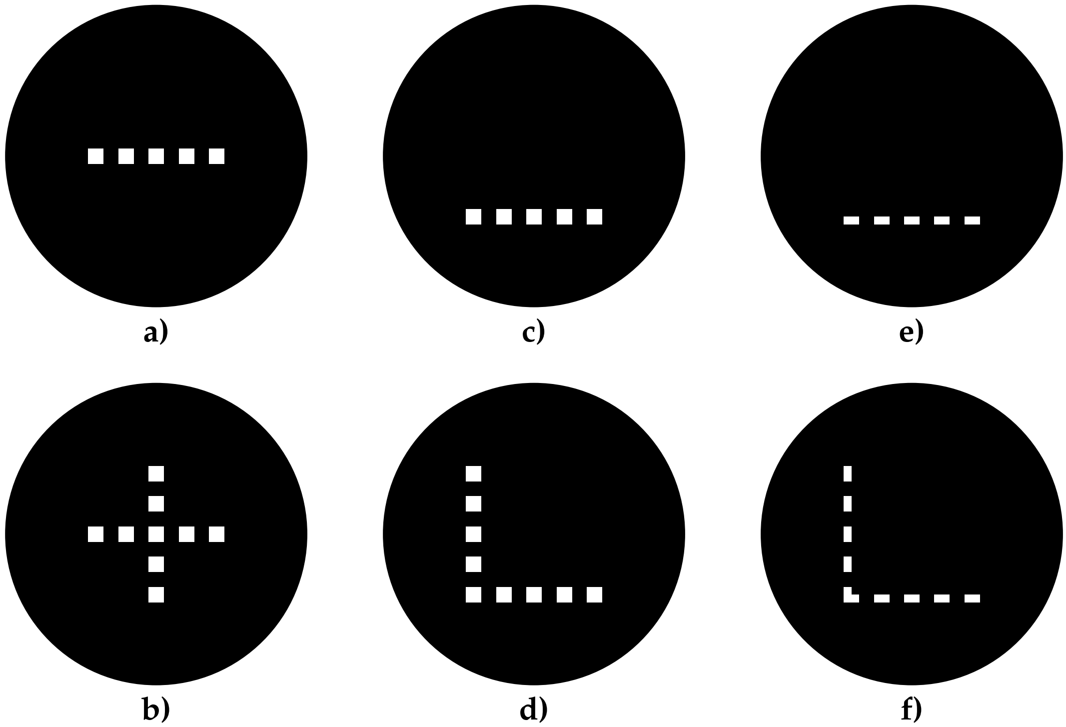

Figure 2. Examples of functional aperture designs.

The on-axis single aperture (Fig. 2a) is the most straightforward approach, allowing a two-dimensional position estimation. Due to its placement near the optical axis, a relatively low impact of diverging from the par-axial approximation can be assumed. This approach can be easily extended for three-dimensional position estimation by adding an orthogonal aperture function (see Fig. 2b). This approach bears the drawback of overlapping aperture images for particles located behind each other along the optical axis. Also, it does not allow the placement of a laser beam within the optical axis to follow the intended backscattering approach (see Fig. 1) without degrading the image quality. While a slight offset of the illumination from the optical axis, enabled by a mirror in the dark area near the aperture function, might be negligible, overlapping aperture images can render a parameter estimation nearly impossible. Therefore, the on-axis aperture approach is only suitable for environments that are relatively sparsely distributed with particles.

To overcome the problem of overlapping aperture images, an off-axis approach, shown in Fig. 2c and d, can be utilized, which was already described by Lee et al. (2015) for a similar setup. The aperture image of a particle within the optical axis scales with the distance to the imaging system, which is in the orthogonal direction to the aperture functions progression. This reduces image overlapping for particles that are a certain distance apart from each other. Therefore, it allows measurements in environments populated more densely with particles.

Building upon the off-axis approach, overlapping aperture images can be further reduced by decreasing the height of light-transmitting blocks of the aperture functions (see Fig. 2e and f). This is possible because the block height does not directly contribute to the frequency of the image but, in turn, reduces the minimal distance that particles can be apart from each other. But this comes at the cost of a reduced light input and might lead to additional diffraction patterns in the aperture images.

2.3. Spectral Properties

The two-dimensional projection of a rectangular transmission grating can be expressed as a binary piecewise-defined function, denoting light-transmitting areas as one $T = 1$ and non-light-transmitting areas as zero $T = 0$:

$$T^{n,w,G}(x) = \begin{cases} 1 & (x \bmod G \leq w) \wedge (0 \leq x) \wedge (x \leq nG) \\ 0 & \text{otherwise} \end{cases}, \tag{1}$$

where G is the grating period length, w is the width of the light-transmitting areas, and n is the number of total periods in the grating function.

For spectral characterization, the Fourier transform of Eq. 1 can be derived:

$$\tilde{T}^{n,w,G}(k) = \mathfrak{F}\left\{T^{n,w,G}(x)\right\} \tag{2}$$

$$= \frac{\mathrm{j}}{k}\left(e^{-\mathrm{j}kw} - 1\right)\sum_{i=0}^{n-1} e^{-\mathrm{j}kiG}, \tag{3}$$

yielding a continuous frequency spectrum, with j as the imaginary unit and k as spatial frequency while preserving the dependency of the grating functions properties. Based on Eq. 3, the power spectral density (PSD) of the grating function can be calculated:

$$S^{n,w,G}(k) = \frac{1}{nG}\left|\tilde{T}^{n,w,G}(k)\right|^2 \tag{4}$$

$$= \frac{1}{nG}\frac{4}{k^2}\left(1 - \cos\left(wk\right)\right)\sum_{i=0}^{n-1}(n-i)\cos\left(kiG\right), \tag{5}$$

which describes the signal power over frequency. It can be used as a performance indicator to optimize the grating function's properties for frequency estimation.

As the goal is to estimate the base frequency of the projected aperture gratings, the PSD at $k_0 = \frac{2\pi}{G}$ has to be maximized. The dependency of $S^{n,w,G}(k_0)$ over the ratio between w and G is shown in Fig. 3 for different period counts n. The maximum PSD for k_0 is achieved at $\frac{w}{G} = 0.5$, which also increases for larger n.

The before-mentioned increase in the PSD with n is a linear relation, shown in Fig. 4 for different $\frac{w}{G}$. Additionally, it can be observed that the gain in PSD per n is increased for $\frac{w}{G} = 0.5$.

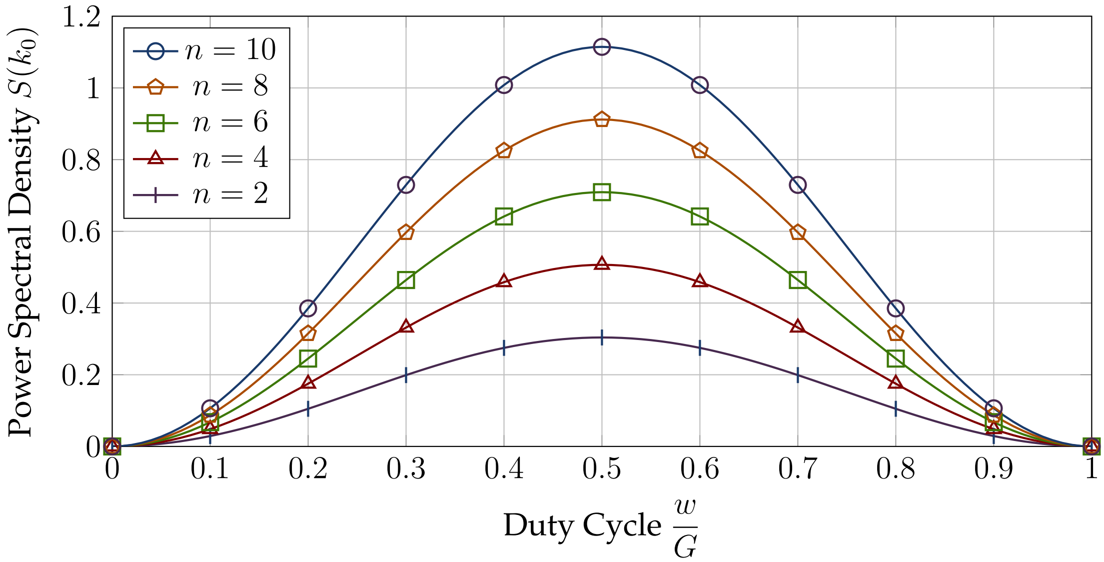

Figure 3. Impact of the duty cycle on the power spectral density of aperture functions.

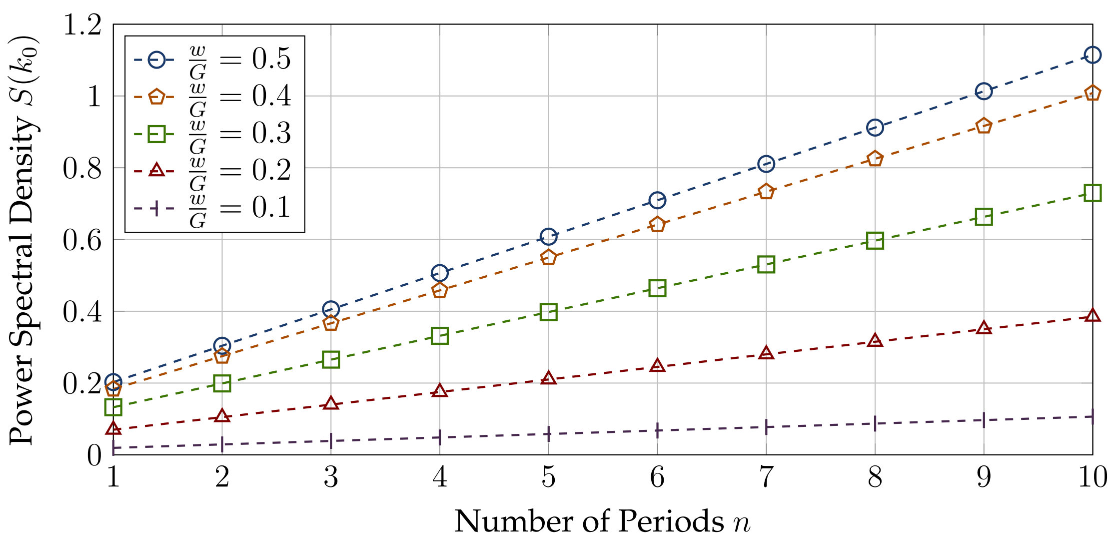

Figure 4. Impact of the number of periods on power spectral density of aperture functions

Two conclusions can be obtained from the above observations:

- The PSD of the transmission grating function is generally maximized at the base frequency if the transmitting and non-transmitting areas are equal in width.
- An increase in grating periods continually increases the PSD.

While the optimal ratio of $\frac{w}{G}$ is easily achievable, the number of grating periods n highly depends on the actual measurement environment and the used system, where the available light, used optics, and imaging sensor properties have to be taken into account.

3. Position Estimation

3.1. Intuitive Approach

3.1.1. Distance

A simple optical system is considered to derive an analytical solution for computing a particle's distance from the period length of the out-of-focus imaged aperture function. It consists of a thin lens with a focal length of f and an aperture mask placed at a distance d in front of it. Figure 5 shows this basic concept of out-of-focus imaging for a single particle lying in the optical axis.

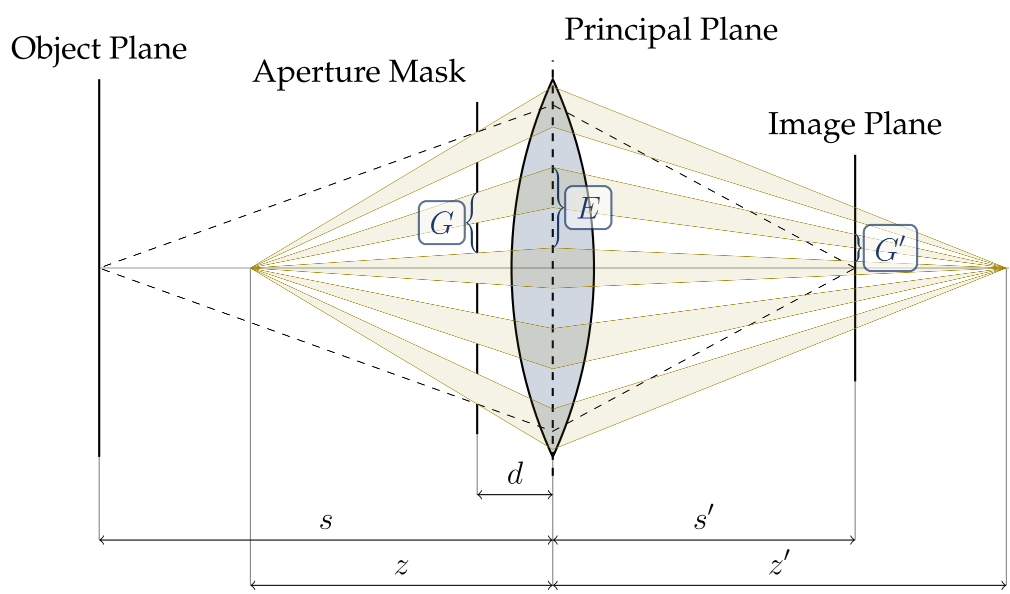

Figure 5. Out-of-focus image creation with a periodic coded aperture for variable distances.

The depicted optical system can be described using the thin lens equation:

$$\frac{1}{f} = \frac{1}{s} + \frac{1}{s'} = \frac{1}{z} + \frac{1}{z'}\,, \tag{6}$$

which provides the connection between the fixed distances to the image plane s' and the resulting focal plane s with the variable particle distance z and its corresponding recessed imaging plane distance z'.

The relationship between the period length of the aperture function, denoted by G, its projection onto the lens plane, denoted by E, and the imaged period length, denoted by G', can be expressed using the intersection theorem:

$$\frac{E}{z} = \frac{G}{z-d} \qquad \text{and} \qquad \frac{E}{z'} = \frac{G'}{z'-s'}\,. \tag{7}$$

Using the central plane of the thin lens as an interface:

$$\frac{Gz}{z-d} = \frac{G'z'}{z'-s'} \tag{8}$$

and applying Eq. 6, allows a closed solution for z:

$$z = \frac{Gs' + G'd}{G' + GM} \qquad \text{with} \qquad M = \frac{s'}{s}\,, \tag{9}$$

which solely depends on G', as all other parameters are fixed within the system. However, Eq. 9 is ambiguous because particle positions with the same distance to the focal plane, regardless of whether they are in front or behind, would yield the same distance. This is because of the change of sign in G' when crossing the focal plane, which cannot be determined with the current design.

3.1.2. Offset

A naive solution for estimating a particle offset x based on the offset of the aperture image x' can be derived by applying the intercept theorem based on the constant sensor distance s' and the estimated particle distance z:

$$x = -\frac{z}{s'}x'\,. \tag{10}$$

This approach, reminiscent of the lever principle, contains a systematic error x'_L, as can already be seen in Fig. 6. The error originates from the distance d between the lens and aperture mask, which is not considered by Eq. 10.

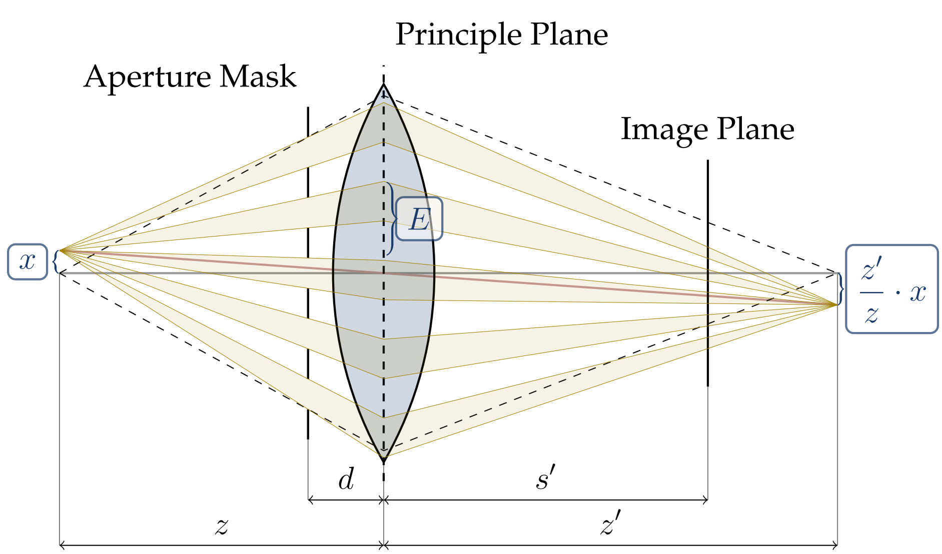

Figure 6. Change of aperture image position due to particle displacement perpendicular to the optical axis.

An extended model for offset estimation can be derived by considering a single opening in the center of a periodic aperture mask. As shown in Fig. 7, a non-zero aperture distance causes the midpoint of the aperture projection to diverge from the center of the lens. This offset, denoted as x_L, is then scaled and propagated to the defocused aperture image.

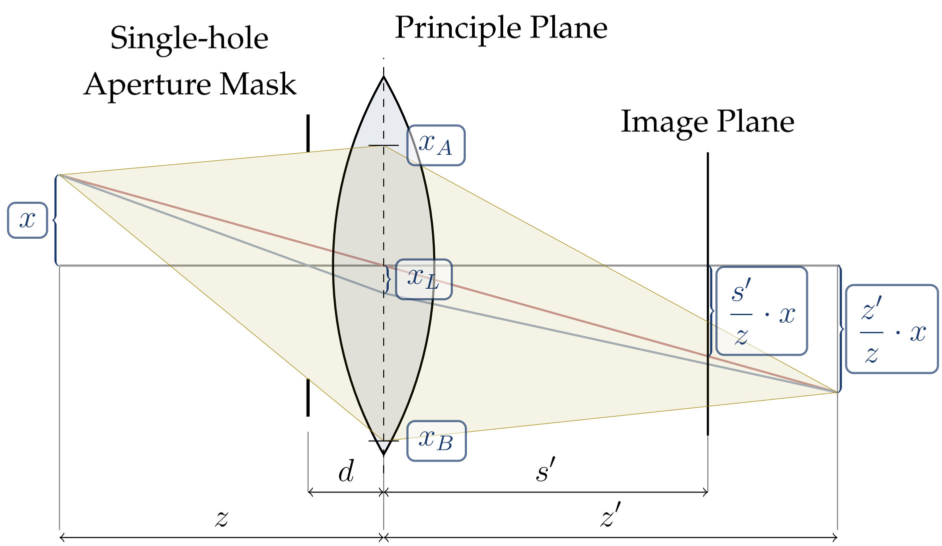

Figure 7. Determination of the aperture image displacement deviation introduced by a non-zero distance between the principal plane and the aperture mask.

The offset in the lens plane x_L can be calculated from the edges of the aperture projection:

$$x_L = \frac{x_A + x_B}{2} = \left(1 - \frac{z}{z-d}\right) x \,, \tag{11}$$

where x_A denotes the upper edge of the projection and x_B the lower edge. Using the intercept theorem, x_L is equal for every other aperture opening, allowing the system to be reduced, as displayed here.

As x_L linearly reduces to zero at a distance of z' from the lens, the relation:

$$\frac{x_L}{E} = \frac{x'_L}{G'} \tag{12}$$

can be used to provide a scaling factor $\frac{G'}{E}$ for x_L in the imaging plane. Together with Eq. 11, a description for the divergence of x'_L from the Eq. 10 can be expressed:

$$x'_L = \frac{G'}{E} x_L \tag{13}$$

$$= \frac{G'}{E}\left(1 - \frac{z}{z-d}\right) x \,. \tag{14}$$

The initial approach in Eq. 10 can now be corrected by superposition with Eq. 14:

$$x' = -\frac{s'}{z}x + x'_L \tag{15}$$

$$= -\frac{s'}{z}x + \frac{G'}{E}\left(1 - \frac{z}{z-d}\right)x \tag{16}$$

$$= -\frac{GM - G'}{G}x\,, \tag{17}$$

resulting in a complete description of the image offset x' based on the physical particle displacement x.

Solving Eq. 17 for x:

$$x = -\frac{G}{G' + GM}x'\,, \tag{18}$$

now allows the estimation of the off-axis particle displacement by analyzing the determined offset of the aperture image and its period length.

3.2. Systematic Approach

3.2.1. Generalized Description of the Optical System

In contrast to the single-lens-approach, an optical system consisting of multiple lenses can be described by a ray transfer matrix (RTF) (Hecht, 2023) with the elements A, B, C, and D. For this study, the optical system described by the RTF is defined from the incident plane of the first lens to the imaging plane, i.e., the imaging sensor. By multiplying the RTF with an incident ray originating from a particle at the position (x, z), the output ray is generated, which consists of a position on the image plane x' and an emergent angle θ':

$$\begin{bmatrix} x' \\ \theta' \end{bmatrix} = \begin{bmatrix} A & B \\ C & D \end{bmatrix} \cdot \begin{bmatrix} x + z\theta \\ \theta \end{bmatrix}\,, \tag{19}$$

of which only the position is used for further calculation.

The Points which describe the lower and the upper part of a single grating period are of particular interest:

$$x'_1 = A\left(x + z\theta_1\right) + B\theta_1 \tag{20}$$

$$x'_2 = A\left(x + z\theta_2\right) + B\theta_2\,, \tag{21}$$

as they allow us to determine the imaged period length:

$$G' = x'_2 - x'_1 \tag{22}$$

$$= \left(Az + B\right)\left(\theta_1 - \theta_2\right)\,, \tag{23}$$

and the aperture image position:

$$x' = \frac{1}{2}\left(x'_1 + x'_2\right) \tag{24}$$

$$= Ax + \frac{1}{2}\left(Az + B\right)\left(\theta_1 + \theta_2\right)\ . \tag{25}$$

These descriptions still need a clear definition of the aperture mask, with its physical period length and placement within the optical system. However, the aperture mask is implicitly introduced by the incident angles θ_1 and θ_2.

3.2.2. Determination of incident rays

Decoupling the aperture mask from the description of the optical systems helps formulate a generalized expression, as it could be placed in front of the optical system, between any of the lenses, or between the last lens and the imaging plane. Therefore, we assume another RTF, which describes the propagation from the incident plane to the plane of the aperture mask:

$$\begin{bmatrix} x' \\ \theta' \end{bmatrix} = \begin{bmatrix} A_G & B_G \\ C_G & D_G \end{bmatrix} \cdot \begin{bmatrix} x + z\theta \\ \theta \end{bmatrix}\ . \tag{26}$$

As the period length of the aperture mask is known, it can be used as a boundary condition:

$$\frac{G}{2} = A_G\left(x + z\theta_1\right) + B_G\theta_1 \tag{27}$$

$$-\frac{G}{2} = A_G\left(x + z\theta_2\right) + B_G\theta_2\,, \tag{28}$$

providing direct access to the incident angles:

$$\theta_1 = \frac{\frac{G}{2} - A_G x}{A_G z + B_G} \tag{29}$$

$$\theta_2 = \frac{-\frac{G}{2} - A_G x}{A_G z + B_G}\,, \tag{30}$$

and subsequently allowing an expression for the desired incident angle sum and difference:

$$\theta_1 - \theta_2 = \frac{G}{A_G z + B_G} \tag{31}$$

$$\theta_1 + \theta_2 = \frac{-2A_G x}{A_G z + B_G}\,. \tag{32}$$

3.2.3. Parameter Estimation

Applying Eq. 31 and Eq. 32 to the preliminary expressions for the period length Eq. 23 and the displacement Eq. 25 respectively, results in a closed expression of the image parameters, dependent from the particle position and the system parameters:

$$G' = \frac{Az + B}{A_G z + B_G} G \tag{33}$$

$$x' = \frac{AB_G - A_G B}{A_G z + B_G} x = \left(A - \frac{G'}{G} A_G \right) x \,. \tag{34}$$

These expressions can be rewritten in terms of the particle position:

$$z = \frac{GB - G'B_G}{G'A_G - GA} \tag{35}$$

$$x = \frac{Gx'}{GA - G'A_G} \,, \tag{36}$$

which can then be computed from the supposedly known system parameters and the determinable aperture image attributes.

3.2.4. Interpretation of System Parameters

While the introduced ray propagation matrices each provide four parameters to describe an optical system, the proposed solutions only require A, B, A_G, and B_G.

The A-parameters generally represent a ratio between the input and output positions of the ray propagation, which can be specified as the negative magnification factor of the optical system (Duarte, 2017). This results in A and A_G being the magnification factor of the optical system with respect to the image plane, i.e., the imaging sensor or the position of the aperture mask, respectively. They can be interpreted as unit-less scaling factors that are primarily, but not entirely, independent of each other, allowing a tuning of the measurement system.

On the other hand, the B-parameters represent the optical length between the input and the output plane of the optical system (Duarte, 2017). As a result, B and B_G are the optical distances from the input plane to the imaging plane and the aperture mask, respectively.

3.2.5. Application to single lens approach

The systematic approach can be concluded by revisiting the single-lens approach depicted in section 3.1 regarding the system parameters. Table 1 summarizes the system parameters and the

Table 1. Applying the generalized approach to a single-lens setup for mask locations before or behind the lens.

Mask before Lens	Mask behind Lens
$A = 1 - \frac{s'}{f} = -\frac{s'}{s} = -M$	
$B = s'$	
$A_G = 1$	$A_G = 1 - \frac{d}{f} = -M_d$
$B_G = -d$	$B_G = d$
$z = \frac{Gs' + G'd}{G' + GM}$	$z = \frac{Gs' - G'd}{-G'M_d + GM}$
$x = -\frac{G}{GM + G'}x'$	$x = -\frac{G}{GM - G'M_d}x'$

resulting position estimation functions for the two cases of placing the aperture mask before or behind the lens.

As previously stated, the parameters A and B are independent of the aperture mask position and equal to the negative magnification factor and the optical distance between the input and imaging planes, respectively.

However, A_G and B_G differ for both configurations and affect the properties of the out-of-focus aperture images. While A_G equals one when placing the aperture before the lens, as there is no diffractive element in the optical path, for the second case, it becomes a negative magnification M_d, which is defined by the aperture position and the focal length of the lens. B_G, on the other hand, B_G signifies, for both cases, the distance of the aperture mask from the lens. The negative sign for an aperture mask placed before the lens originates from the definition of the system. A backward propagation is needed as the incoming rays are strictly defined from the particle to the lens plane.

It can be stated that the placement of the aperture mask has a significant impact on the system behavior. By adjusting the aperture position, and therefore A_G and B_G, the system's dynamic can be tailored to the target environment without changes to the underlying imaging system.

3.3. Verification

3.3.1. Simulation Environment

A simulation approach is adopted to verify the position estimation models derived above. In contrast to an experimental setup, this allows complete control over all geometric parameters of the imaging system, providing a ground truth for the verification. The simulation environment was established using the Python library *diffractsim* (De la Fuente, n.d.), which is based on diffraction theory to compute the propagation of light and diffractive optical elements and was customized to support point light sources. Using diffraction theory has two advantages. Firstly, the results are primarily decoupled from ray optics, which serves as the foundation for the mathematical descriptions in 3.1.1 and 3.1.2, and secondly, it allows the observation of effects based on wavelength, diffraction, and interference on the image and estimation quality. Monochromatic and polychromatic wavefields are supported by *diffractsim*. Still, it has to be noted that the superposition of a series of monochromatic simulations at discrete wavelengths is the foundation of the polychromatic simulation. Therefore, the polychromatic mode is not directly interpretable as a simulation of incoherent white light.

A simulation environment consisting of a single lens was constructed to verify the distance estimation, derived in section 3.1.1. The lens had a diameter of $30\,\mathrm{mm}$ and a focal length of $300\,\mathrm{mm}$. The Sensor was placed at a distance of $600\,\mathrm{mm}$ from the lens with a horizontal width of $8\,\mathrm{cm}$ and a resolution of $16\,384$ px. A grating function with 5 periods and a period length of $4\,\mathrm{mm}$ was placed at a distance of $5\,\mathrm{mm}$ in front of the lens. Simulations were performed for particle distances between $200\,\mathrm{mm}$ and $600\,\mathrm{mm}$ and offsets between $0\,\mathrm{mm}$ and $5\,\mathrm{mm}$ in the monochromatic mode, at $450\,\mathrm{nm}$, as well as in the polychromatic mode.

A series of example images from the polychromatic simulation at different particle distances is shown in Fig. 8.

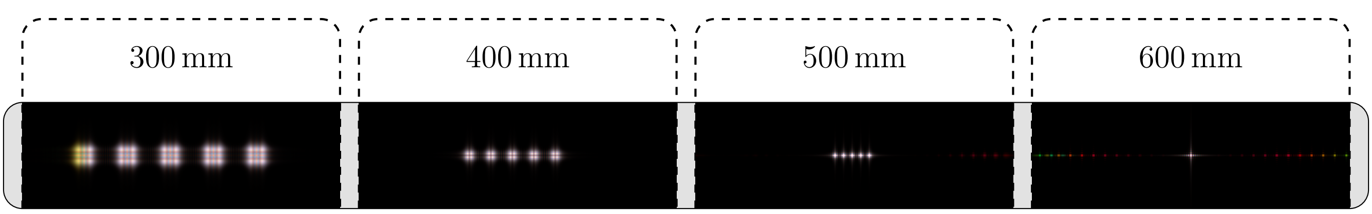

Figure 8. Example aperture images, generated by *diffractsim*, for different point source distances

The Fast Fourier Transform with an additional zero padding is used to determine the period length of the aperture images, while a cross-correlation extended Gaussian interpolation allows the offset estimation.

3.3.2. Results

The relative error of the distance estimations for particles within the optical axis is shown in Fig. 9.

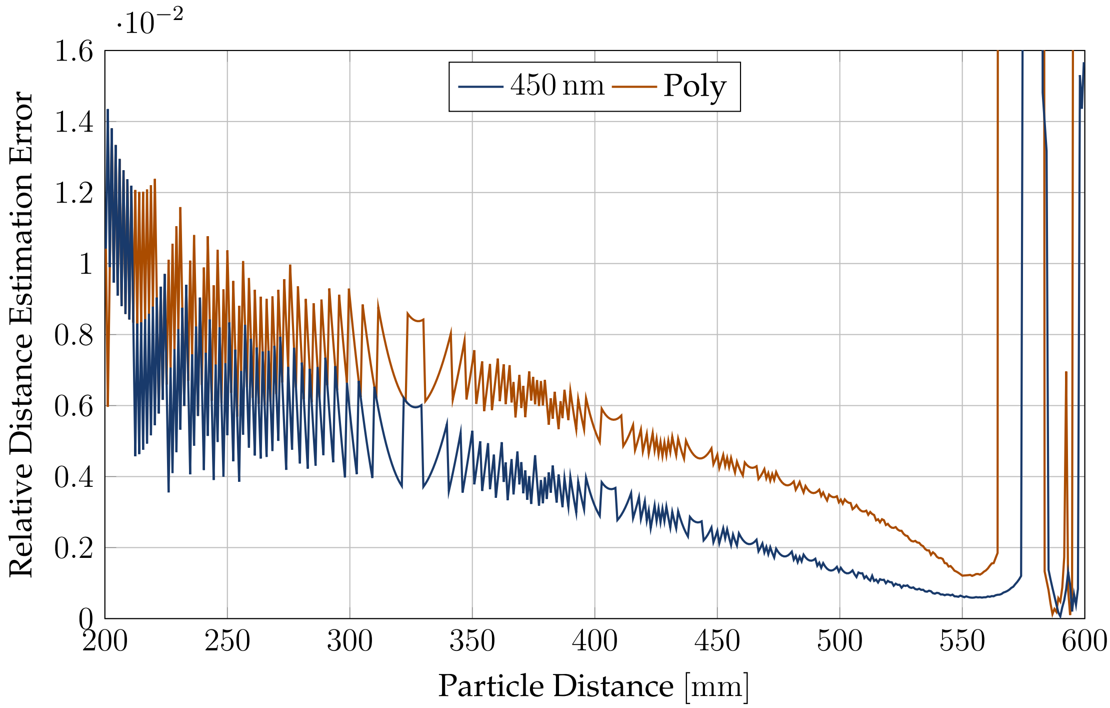

Figure 9. Distance estimation performed on simulated aperture images.

It is visible that the relative error of the distance estimation remains below 10^{-2} for the majority of the observed distance range. For shorter distances, the relative error increases as the aperture images become larger, exceeding the boundary of the imaging plane. Also, the quality of the frequency estimation degrades due to additional patterns originating from diffraction and interference. Likewise, the estimation quality can be degraded for larger distances. On the one hand, this is tied to the wavelength and can be tracked down to a numerical error in the diffraction theory computation. On the other hand, when approaching the object plane of the imaging system, the period length of the aperture images becomes undeterminable as the image reduces to a point.

Another observation that can be made is that using a monochromatic source at $450\,\mathrm{nm}$ shows a better overall performance than using a polychromatic source. This is because the polychromatic simulation is a superposition of multiple monochromatic sources. It contains sources of larger wavelengths, causing considerable diffraction patterns in the aperture image, which degrade the frequency estimation quality.

Figure 10 shows the relative error of estimations of particle offsets from the optical axis.

It is visible that the estimation errors largely align between the poly- and the monochromatic simulation. A significant difference can be observed only for shorter distances, where the frequency es-

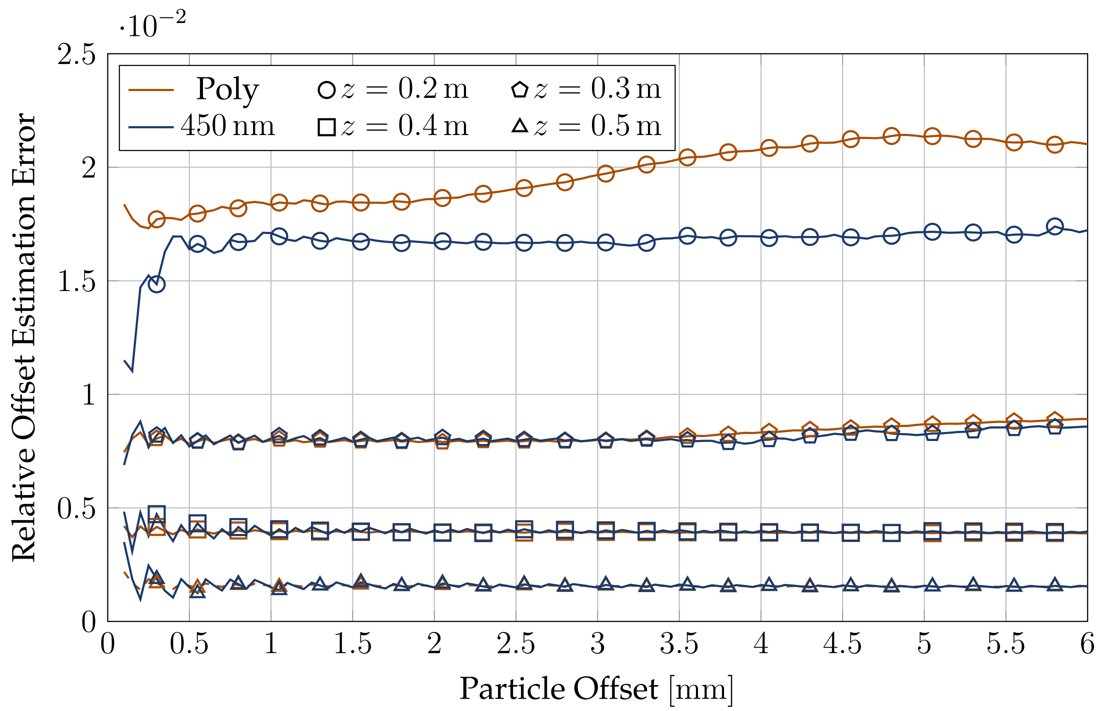

Figure 10. Offset estimation performed on simulated aperture images.

timation error dominates. Further, the relative errors stay nearly constant over the whole offset for a fixed distance and decrease with distance. The dynamic behavior of the aperture image creation can explain this. The imaged period length changes at a slower rate for larger distances. Still, it is generally smaller, allowing a better estimation of the aperture image offset by cross-correlation.

4. Calibration

4.1. Algorithms

While the position estimation functions presented in Section 3 work appropriately for an imaging system with precisely known geometric parameters, they become difficult to handle in practice. Regardless if a single-lens-system as shown in Fig. 5 or a commercial camera lens containing multiple lenses is used, the parameters s', G, d, and s can't be known beforehand at a level of precision that ensures a reliable estimation. Therefore, a calibration method is needed that relies on a target particle that can be positioned freely.

A least squares approach is used to obtain the geometric parameters of the imaging system. It is derived by restructuring Eq. 35 to:

$$z = \frac{B}{A_G} G G'^{-1} - \frac{B_G}{A_G} + \frac{A}{A_G} G z G'^{-1}\,, \tag{37}$$

leading to a linear system of equations of:

$$\underbrace{\begin{bmatrix} z_1 \\ \vdots \\ z_n \end{bmatrix}}_{\mathbf{z}} = \underbrace{\begin{bmatrix} G_1'^{-1} & -1 & z_1 G_1'^{-1} \\ \vdots & \vdots & \vdots \\ G_n'^{-1} & -1 & z_n G_n'^{-1} \end{bmatrix}}_{\mathbf{M}} \cdot \underbrace{\begin{bmatrix} \dfrac{B}{A_G} G \\ \dfrac{B_G}{A_G} \\ \dfrac{A}{A_G} G \end{bmatrix}}_{\boldsymbol{\mu}} , \tag{38}$$

for a series of n target positions on the calibration setup. As the vector of target distances $\mathbf{z}$ and the matrix $\mathbf{M}$ are generated from either set or measured values, the solution for $\boldsymbol{\mu}$, which contains the needed geometric parameters of the imaging system, is computed by performing the least squares method:

$$\boldsymbol{\mu} = \left(\mathbf{M}^\top \mathbf{M}\right)^{-1} \mathbf{M}^\top \mathbf{z} \,. \tag{39}$$

Equation 35 is then expressed in terms of the components of $\boldsymbol{\mu}$:

$$z = \frac{\mu_1 + \mu_2 G'}{G' + \mu_3} \,. \tag{40}$$

The optical system parameters for determining the lateral offset can be obtained using the above-mentioned approach. Restructuring Eq. 36 yields:

$$x = x \frac{A}{A_G} G G'^{-1} - x' \frac{1}{A_G} G G'^{-1} \tag{41}$$

leading to the linear system of equations:

$$\underbrace{\begin{bmatrix} x_1 \\ \vdots \\ x_n \end{bmatrix}}_{\mathbf{x}} = \underbrace{\begin{bmatrix} x_1 G_1'^{-1} & -x'_1 G_1'^{-1} \\ \vdots & \vdots \\ x_n G_n'^{-1} & -x'_n G_n'^{-1} \end{bmatrix}}_{\mathbf{N}} \cdot \underbrace{\begin{bmatrix} \dfrac{A}{A_G} G \\ \dfrac{1}{A_G} G \end{bmatrix}}_{\boldsymbol{\nu}} , \tag{42}$$

which can also be solved for $\boldsymbol{\nu}$ using the least squares approach:

$$\boldsymbol{\nu} = \left(\mathbf{N}^\top \mathbf{N}\right) \mathbf{N}^\top \mathbf{x} \,. \tag{43}$$

Equation 36 is then expressed in terms of the components of $\boldsymbol{\nu}$:

$$x = -\frac{\nu_2}{G' - \nu_1} x' \,. \tag{44}$$

It is also possible to use these calibration algorithms with G' and x' in terms of pixels (unit: px) instead of length units, which would require a conversion based on the pixel size of the used imaging sensor. This, in turn, allows the usage of input values in px for estimating the distance and lateral displacement, eliminating the otherwise needed conversion step from the evaluation procedure.

4.2. Calibration Setup

The target in the calibration setup consists of a high-power LED covered by a pinhole with a diameter of $200\,\mathrm{\mu m}$. Therefore, the pinhole position is equivalent to the position of an illuminated particle. The target is mounted on two orthogonal motorized linear axes, allowing it to be positioned freely in two dimensions.

An IDS uEye Camera (UI306xCP-M), including a Sony IMX174 B/W imaging sensor and a Kowa LM35HC-V C-Mount lens, with a focal length of $35\,\mathrm{mm}$ serves as an imaging system. A single-axis offset aperture mask with five periods and a period length of $4\,\mathrm{mm}$ is directly mounted using a threaded ring in front of the lens. The object plane is shifted as far away from the camera as possible to ensure a defined state throughout the calibration process and prevent the target from crossing it.

4.3. Verification

Using the described calibration setup, a series of images is created, where the target is placed at distances ranging from $130\,\mathrm{mm}$ to $584\,\mathrm{mm}$ in steps of $0.4\,\mathrm{mm}$ and laterally displaced between $0\,\mathrm{mm}$ and $10\,\mathrm{mm}$ in steps of $0.2\,\mathrm{mm}$. We determined the period lengths using a zero-padded FFT and the image displacements by cross-correlation with Gaussian interpolation to enable sub-pixel accuracy. The relative errors of the position estimation results are represented in Fig. 11. For a better understanding of the global behavior of the position estimation, the relative root mean square errors (RRMSE) in the distance and offset direction are also shown.

Figure 11a shows the relative error of distance estimations over the observation area of the calibrated model on the same image data set. Over large areas, the distance estimations were performed with an uncertainty below $1\,\%$, but the overall area is disturbed by two distinct error patterns. The most significant are coil-like structures, which appear closer to the imaging system and lean in the lateral direction. These are most likely introduced due to the comparably large pinhole and the structured light-emitting area of the high-power LED used in the setup. When moving the LED in the lateral direction, different regions of the LED are visible through the pinhole, resulting in intensity fluctuations in the aperture images and, therefore, inaccuracies in the frequency estimation. The other visible pattern is a sweep-like structure in the background caused by the

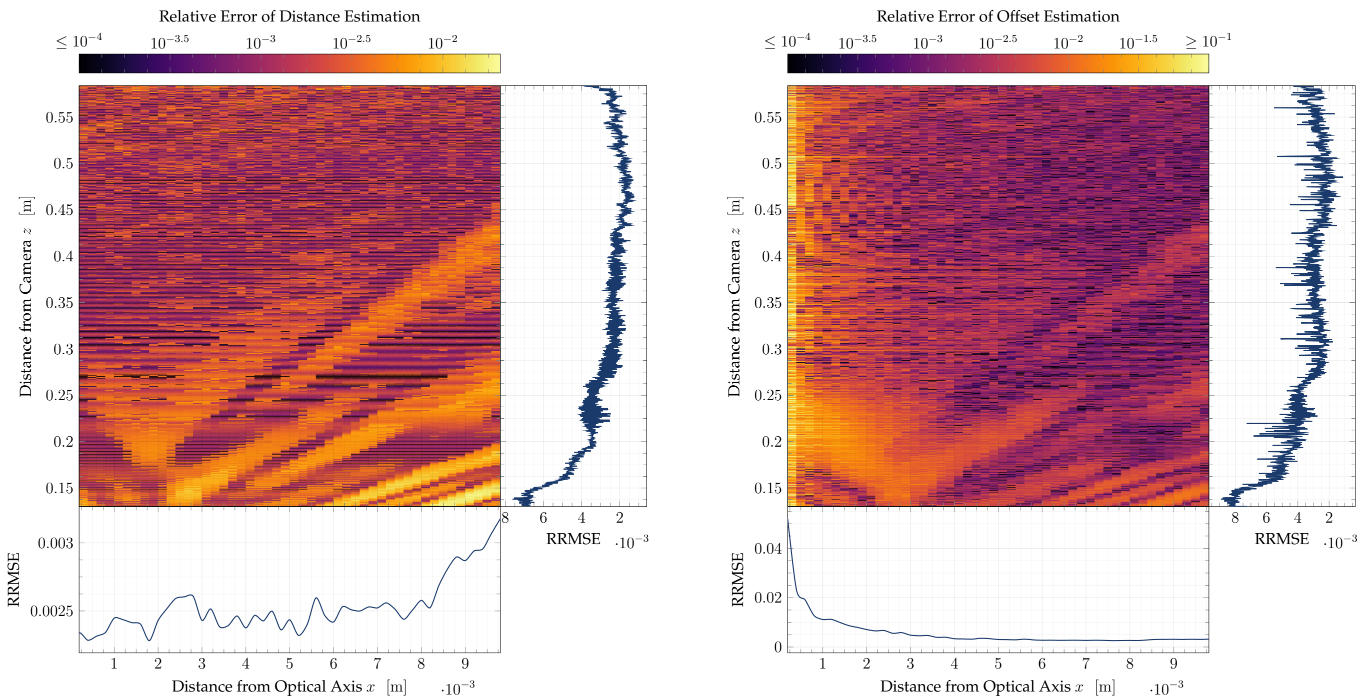

(a) Distance Estimation

(b) Offset Estimation

Figure 11. Relative Errors of two-dimensional Position Estimations performed by a calibrated Imaging System.

discretized frequency estimation. It could be further reduced by increasing the zero-padding used for the FFT or interpolating the frequency peak within the spectrum.

The relative error of lateral displacement estimations depending on distance is shown in Fig. 11b. As well as for the distance estimation, large areas of errors far below $1\,\%$, and the beforementioned error patterns are visible. The relative estimation error is also increased for smaller lateral displacements due to errors in determining period length and image displacement, which become dominant for small displacement amounts.

5. Measurement

5.1. Setup

The described measurement principle was applied in an experiment inside the drag channel at SVA Potsdam on a scale model of a bulk carrier ship. It was aimed at measuring the velocity field between the duct and the propeller of the model ship, an area of observation that was accessible from the top of the ship through an acrylic window (see Fig. 12a).

The measurement setup, a crucial component of this experiment, consisted of two cameras. These cameras were calibrated using the least squares approach shown in section 4 and were set to measure a single velocity component each, placed perpendicular to each other. This architecture was chosen to increase the achievable framerate by reducing the lines of the region of interest on the camera sensors. A $450\,\mathrm{nm}$ continuous wave diode laser was placed between the cameras to illuminate the measurement volume (see Fig. 12b). It was pointed into the measurement volume at a slight angle to reduce the amount of visible reflections on the interfaces of the viewing window.

The entire setup was placed on two perpendicular linear motor axes, which allowed adjusting the distance and the position parallel to the viewing window. The laser was placed at a particular position for each measurement cycle, where distances and velocities of particles crossing the laser beam were measured. The two-dimensional velocity field between the duct and the propeller could be reconstructed by repeating this process for different laser positions.

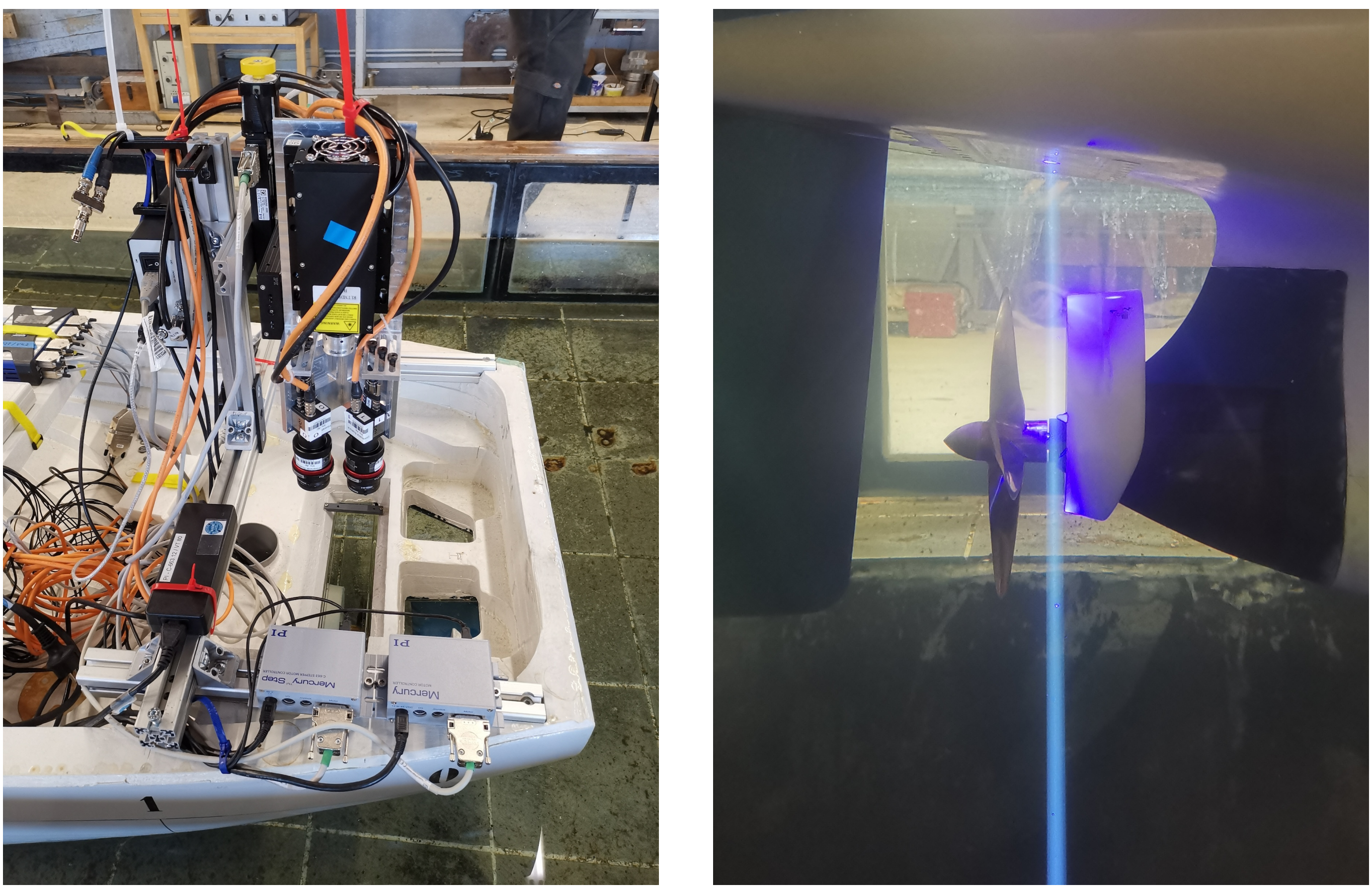

(a) Two-Camera measurement Setup

(b) Laser placed between duct and propeller

Figure 12. Measurement setup used on a model ship in a drag channel.

5.2. Results

The velocity field captured within one of the experiments is shown in Fig. 13 for the main velocity component, which is pointed parallel to the model's longitudinal axis in the backward direction

(Fig. 13a), and the horizontal velocity component (Fig. 13b). They are composed of 18 vertical lines, i.e., laser positions, captured in measurement cycles with a duration of $30\,\mathrm{s}$, where the model was dragged through the channel at a speed of $1.2\,\mathrm{m\,s^{-1}}$. Each dot represents the average velocity component within a specific depth range at the observed particles' average position.

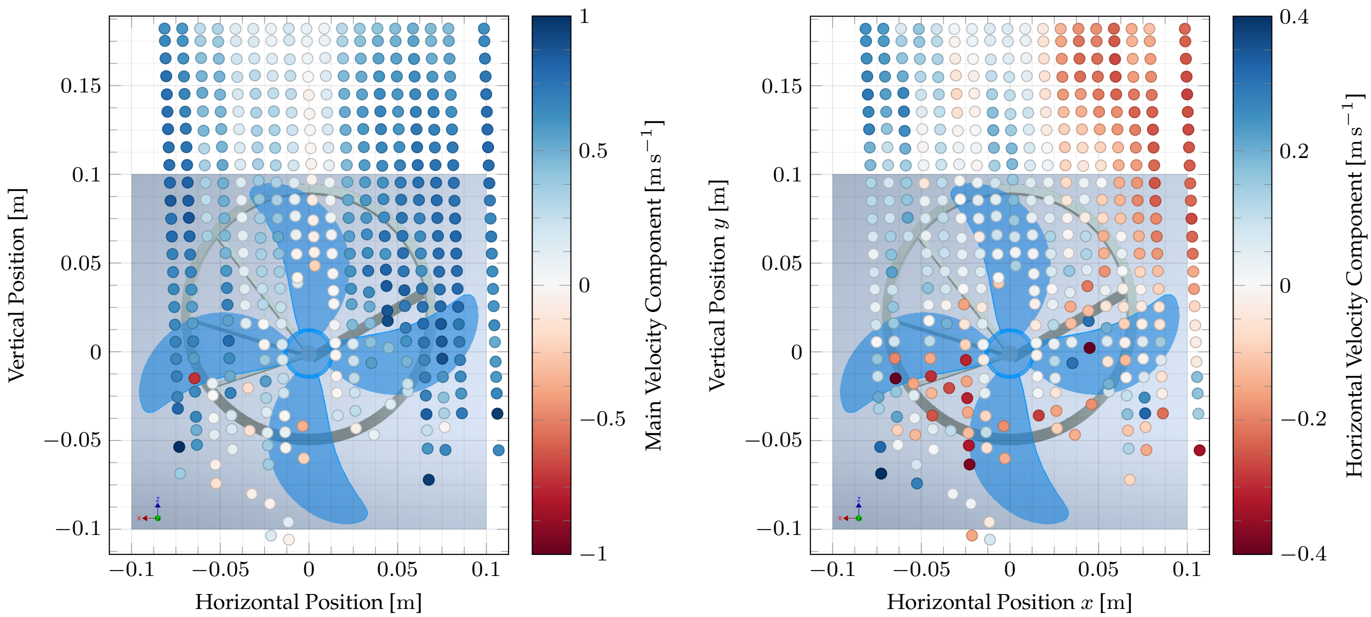

(a) Main velocity component

(b) Horizontal velocity component

Figure 13. Measurement Results

For the main velocity component (see Fig. 13a), lower velocities are observed towards the center of the model and near the viewing window. This observation is significant, as it aligns with the expectation that the hull of the ship model slows down the flow of the surrounding water, validating our experimental setup and measurement principle.

The horizontal velocity component (see Fig. 13b) exhibits a dominant flow towards the ship's center. The curvature of the hull of the model ship primarily influences this flow pattern.

During the measurement, we encountered a decrease in valid measurement values with an increased distance to the measurement system. This decrease was primarily due to the low intensity of the backscattering radiation from the particles, which was accompanied by the overall low particle density within the media. To ensure the accuracy of our data, we only considered particles detected by both cameras to contribute to a valid measurement value, adding another layer of complexity to our data collection process.

6. Conclusion

In practical terms, the results of this work provide a revised approach to out-of-focus Particle Image Velocimetry that allows us to perform measurements in an environment with only a single optical access window. The mathematical model was derived using basic ray optical theory and verified by diffraction-theoretical simulation. Also, a calibration procedure was proposed, making the measurement principle applicable to a wide range of optical system configurations without further modifications. Additionally, the concept was applied to a real-world fluid-mechanic experiment, where reasonable results were yielded.

References

De la Fuente, R. (n.d.). *diffractsim: A flexible python diffraction simulator.* Retrieved from `https://github.com/rafael-fuente/diffractsim` doi: 10.5281/zenodo.6843673

Duarte, F. J. (2017). *Tunable laser optics*. CRC Press.

Hecht, E. (2023). *Optik*. Berlin, Boston: De Gruyter Oldenbourg. Retrieved 2024-04-20, from `https://doi.org/10.1515/9783111025599` doi: doi:10.1515/9783111025599

Lee, E., Chae, E., Cheong, H., Jeon, S., & Paik, J. (2015, Aug). Depth-based defocus map estimation using off-axis apertures. *Opt. Express*, *23*(17), 21958–21971. Retrieved from `https://opg.optica.org/oe/abstract.cfm?URI=oe-23-17-21958` doi: 10.1364/OE.23.021958

Pentland, A. P. (1987). A new sense for depth of field. *IEEE transactions on pattern analysis and machine intelligence*, *9*(4), 523–531.

Pereira, F., & Gharib, M. (2002). Defocusing digital particle image velocimetry and the three-dimensional characterization of two-phase flows. *Measurement Science and Technology*, *13*(5), 683.

Pereira, F., Gharib, M., Dabiri, D., & Modarress, D. (2000). Defocusing digital particle image velocimetry: a 3-component 3-dimensional dpiv measurement technique. application to bubbly flows. *Experiments in fluids*, *29*(Suppl 1), S078–S084.

Pereira, F., Lu, J., Castano-Graff, E., & Gharib, M. (2007). Microscale 3d flow mapping with μddpiv. *Experiments in fluids*, *42*, 589–599.

Raffel, M., Willert, C. E., Scarano, F., Kähler, C. J., Wereley, S. T., & Kompenhans, J. (2018). *Particle image velocimetry : A practical guide* (Array ed.) [Online-Ressource]. Cham: Springer. Retrieved from `https://doi.org/10.1007/978-3-319-68852-7` (Online-Ressource (XXVI, 669 p. 434 illus., 164 illus. in color, online resource))

Steinmetz, T., Schaeper, M., Kleinwächter, A., Otto, J., Richter, A., Poosch, R., & Damaschke, N. (2023). Time-resolved determination of velocity fields on the example of a simple water channel flow, using a real-time capable fpga-based camera platform. *Experiments in Fluids*, *64*(4), 73. Retrieved from `https://doi.org/10.1007/s00348-023-03617-8` doi: 10.1007/s00348-023-03617-8

Willert, C., & Gharib, M. (1992). Three-dimensional particle imaging with a single camera. *Experiments in Fluids*, *12*, 353–358.